

Analysis of shock motion in shockwave and turbulent boundary layer interaction using direct numerical simulation data

MINWEI WU AND M. PINO MARTÍN

Department of Mechanical and Aerospace Engineering, Princeton University,
Princeton, NJ 08544, USA

(Received 22 February 2007 and in revised form 10 August 2007)

Direct numerical simulation data of a Mach 2.9, 24° compression ramp configuration are used to analyse the shock motion. The motion can be observed from the animated DNS data available with the online version of the paper and from wall-pressure and mass-flux signals measured in the free stream. The characteristic low frequency is in the range of (0.007–0.013) U_∞/δ , as found previously. The shock motion also exhibits high-frequency, of $O(U_\infty/\delta)$, small-amplitude spanwise wrinkling, which is mainly caused by the spanwise non-uniformity of turbulent structures in the incoming boundary layer. In studying the low-frequency streamwise oscillation, conditional statistics show that there is no significant difference in the properties of the incoming boundary layer when the shock location is upstream or downstream. The spanwise-mean separation point also undergoes a low-frequency motion and is found to be highly correlated with the shock motion. A small correlation is found between the low-momentum structures in the incoming boundary layer and the separation point. Correlations among the spanwise-mean separation point, reattachment point and the shock location indicate that the low-frequency shock unsteadiness is influenced by the downstream flow. Movies are available with the online version of the paper.

1. Introduction

The boundary layer flow over a compression ramp is one of the canonical shock wave and turbulent boundary layer interaction (STBLI) configurations that have been studied extensively in experiments since the 1970s. From this body of work, we have learned that the shock motion has a frequency much lower than the characteristic frequency of the incoming boundary layer. The time scale of the low-frequency motion is $O(10\delta/U_\infty-100\delta/U_\infty)$ as reported in various experiments such as Dolling & Or (1985), Selig (1988), Dussauge, Dupont & Debiève (2006), and Dupont, Haddad & Debieve (2006). In contrast, the characteristic time scale of the incoming boundary layer is $O(\delta/U_\infty)$. The scale to normalize the frequency of the shock motion is still under debate. However, Dussauge *et al.* (2006) found that using $St_L = fL/U_\infty$, where L is the streamwise length of the mean separation bubble, experimental data (covering a wide range of Mach numbers and Reynolds numbers and various configurations) can be grouped between $St_L = 0.02$ and 0.05.

Also, the cause of the low-frequency motion is still an open question. Plotkin (1975) proposed a damped spring model for the shock motion. Andreopoulos & Muck (1987) concluded that the shock motion is driven by the bursting events in the incoming boundary layer. However, Thomas, Putnam & Chu (1994) found no connection between the shock motion and bursting events in the incoming boundary

M	Re_θ	θ (mm)	δ^* (mm)	δ (mm)	δ^+	C_f
2.9	2300	0.38	1.80	6.4	320	0.0021

TABLE 1. Inflow conditions (defined at $x = -9\delta$) for the DNS. The Mach number, Reynolds number based on the momentum thickness, displacement thickness, boundary layer thickness, boundary layer thickness in wall variables, and skin friction are given, from left to right.

layer. Erengil & Dolling (1991) found that there was a correlation between certain shock motions and pressure fluctuations in the incoming boundary layer. Beresh, Clemens & Dolling (2002) found that positive velocity fluctuations near the wall correlate with downstream shock motion. Pirozzoli & Grasso (2006) analysed direct numerical simulation (DNS) data of a reflected shock interaction and proposed that a resonance mechanism might be responsible for the shock unsteadiness. Dussauge *et al.* (2006) suggested that the three-dimensional nature of the interaction in the reflected shock configuration is a key to understanding the shock unsteadiness. Ganapathisubramani, Clemens & Dolling (2007a) proposed that very long alternating structures of uniform low- and high-speed fluid in the logarithmic region of the incoming boundary layer are responsible for the low-frequency motion of the shock. These so-called ‘superstructures’ have been observed in supersonic boundary layers by Samimy, Arnette & Elliott (1994), Ganapathisubramani, Clemens & Dolling (2006), and are also evident in the elongated wall-pressure correlation measurements of Owen & Horstmann (1972). Superstructures have also been observed in the atmospheric boundary layer experiments of Hutchins & Marusic (2007) and confirmed in DNS of supersonic boundary layers by Ringette, Wu & Martin (2008).

Wu & Martin (2007) presented a direct numerical simulation of STBLI for a 24° compression ramp configuration at Mach 2.9 and Reynolds number based on momentum thickness of 2300. They validated the DNS data against the experiments of Bookey *et al.* (2005) at matching flow conditions, and they illustrated the existence of the superstructures. In this paper, we use the Wu & Martin (2007) data to analyse the shock unsteadiness. While in previous experiments the shock motion is usually inferred from measurements the wall pressure, our analyses of the shock motion are carried mainly in the outer part of the boundary layer and in the free stream. This is because the Reynolds number that we consider is much lower than those in typical experiments. Consequently, viscous effects are more prominent, the shock does not penetrate as deeply as in higher Reynolds number flows, and the shock location is not well-defined in the lower half of the boundary layer. In addition, the motion of the separation bubble is studied. Table 1 lists the inflow boundary layer conditions, and figure 1 shows the computational domain and the coordinate system. Note that we use z_n to denote the wall-normal coordinate and prime symbols to denote fluctuating quantities. Statistics are gathered over $300\delta/U_\infty$. The characterization of the shock motion and the unsteadiness of the separation bubble are given in §§ 2 and 3. A discussion is presented in § 4. Finally, conclusions are drawn in § 5.

2. Shock motion

Figure 2(a) plots three wall-pressure signals measured at three streamwise locations upstream of the ramp corner (the corner is located at $x = 0$) along the spanwise centre line. In the incoming boundary layer at $x = -6.9\delta$, the normalized magnitude is around unity with small fluctuations. At $x = -2.98\delta$, which is the mean separation point (defined as the point where the mean skin friction coefficient changes sign from

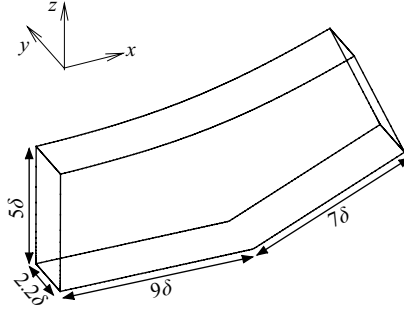
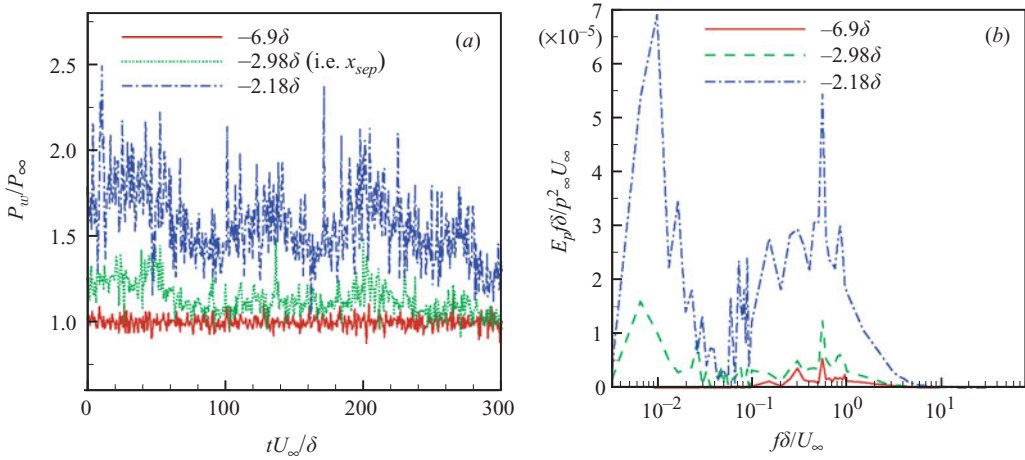


FIGURE 1. Computational domain of the DNS and coordinate system.

FIGURE 2. (a) Wall-pressure signals and (b) wall-pressure energy spectra at different streamwise locations relative to the ramp corner with $y = 1.1\delta$. From Wu & Martin (2007).

positive to negative), the magnitude fluctuates between 1 and 1.2. At $x = -2.18\delta$, the magnitude oscillates between 1.5 and 2. The corresponding premultiplied energy spectra are plotted in figure 2(b). At the mean separation point, the peak frequency is $0.007U_\infty/\delta$. At $x = -2.18$, the peak is at $0.01U_\infty/\delta$. Let us define the Strouhal number $St_L = fL/U_\infty$, where L is the length of the mean separation bubble ($L = 4.2\delta$ in the DNS). The range of St_L is 0.03–0.042, which is consistent with the range given by Dussauge *et al.* (2006).

Contours of the magnitude of the gradient of pressure on streamwise–spanwise planes are plotted in figures 3. Two instantaneous flow fields are plotted at $z_n = 0.9\delta$ and 2δ away from the wall. At $z_n = 2\delta$, figure 3(a, b), the shock is nearly uniform in the spanwise direction. The streamwise movement of the shock is roughly 1δ . Figure 3(c, d) plots the same times at a plane closer to the wall. We observe a wrinkling of the shock in the spanwise direction, with an amplitude of about 0.5δ . At $z_n = 0.9\delta$, the shock also moves in the streamwise direction in the same manner as shown in figure 3(a, b). The amplitude of the motion in the streamwise direction is twice that of the spanwise wrinkling.

We analyse the shock motion in the context of these two aspects. One is that the shock wrinkles along the spanwise direction. The other corresponds to the larger amplitude motion upstream and downstream. The motion that is inferred from the wall-pressure signal in figure 2 results from the combination of these two aspects.

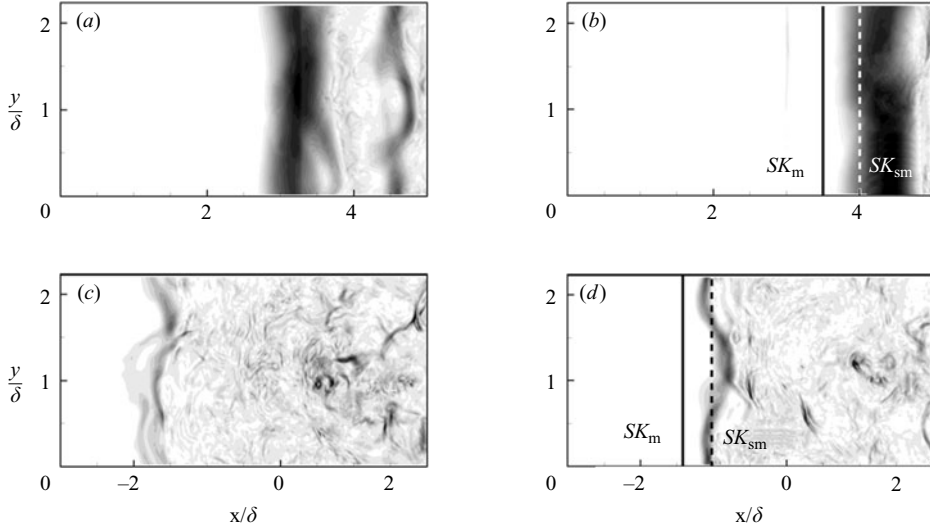


FIGURE 3. Contours of $|\nabla p|$ showing the shock location for two flow realizations separated by $50\delta/U_\infty$ at $z_n = 2\delta$ (*a, b*) and $z_n = 0.9\delta$ (*c, d*). Dark indicates large gradient. See also movie 1 available with the online version of the paper.

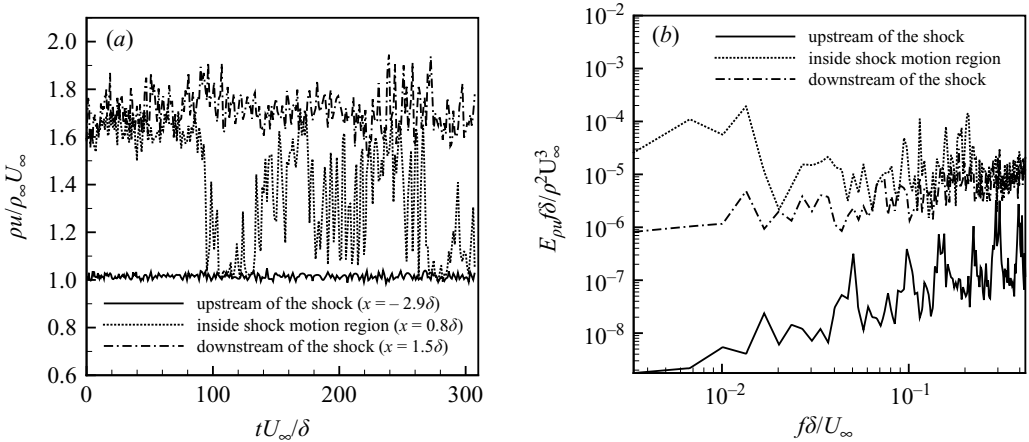


FIGURE 4. (*a*) Mass-flux signals and (*b*) corresponding premultiplied energy spectra measured for different streamwise locations at $z_n = 2\delta$. From Wu & Martín (2007).

However, the low-frequency motion is related to the large-amplitude streamwise motion rather than to the spanwise wrinkling. This can be seen from the mass-flux signals measured in the free stream as shown in figure 4. The signals are measured at different streamwise locations (upstream, inside, and downstream of the shock motion region) at a distance of 2δ away from the wall along the centreline of the computational domain. In figure 4(*a*), the mass-flux signal measured inside the region of shock motion oscillates between those measured upstream and downstream, indicating that the shock is moving upstream and downstream of that point. The premultiplied energy spectra plotted in figure 4(*b*) show that the characteristic low-frequency range is in the range $(0.007\text{--}0.013) U_\infty/\delta$, which is roughly the same as that given by the wall-pressure signals in figure 2(*b*).

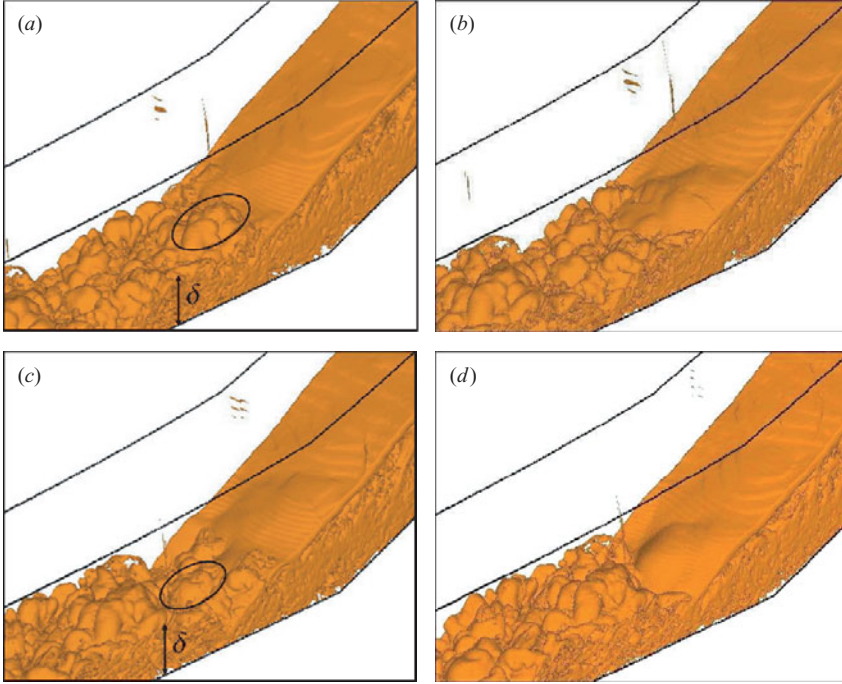


FIGURE 5. Iso-surface of $|\nabla\rho|=2\rho_\infty/\delta$ showing structures in the incoming boundary layer passing through the shock. Temporal spacing between each frame is δ/U_∞ . See movie 2 available with the online version of the paper.

Figure 5 plots normalized iso-surfaces of $|\nabla\rho|$ for four consecutive instantaneous flow fields. The structures in the incoming boundary layer and the shock can be seen. Two structures are highlighted in figures 5(a) and 5(c). For an adiabatic wall, as in the DNS, these structures contain low-density low-speed fluid. As these structures pass through the shock, the shock curves upstream, resulting in spanwise wrinkling of the shock as shown in figures 5(b) and (d). From the data animation, the characteristic frequency of spanwise wrinkling is $O(U_\infty/\delta)$.

To analyse the streamwise unsteadiness, we introduce two definitions for the averaged shock location. First, the spanwise-mean location, SK_{sm} , in which the instantaneous location is defined as the point where the pressure rises to $1.3p_\infty$ in the streamwise direction. Thus, SK_{sm} is a function of time and z_n . Second, the absolute mean shock location, SK_m , which is computed by spanwise and temporal averaging the instantaneous shock location. In turn, SK_m is only a function of z_n . Figures 3(b) and 3(d) show SK_{sm} and SK_m locations.

The correlation with time lag between the pressure at SK_{sm} and the mass flux in the undisturbed incoming boundary layer (5δ upstream of the ramp corner) is plotted in figure 6(a), where the correlation between two fluctuating signals is defined as

$$R_{ab}(\tau) = \langle a(x_1, t)b(x_2, t + \tau) \rangle / \sqrt{\langle a(x_1)^2 \rangle \langle b(x_1)^2 \rangle}, \quad (1)$$

where τ is the time delay. Using SK_{sm} in the correlation removes the effect of the streamwise motion. The local correlation is computed first using data on a given spanwise plane and then the local correlations are spanwise averaged. The signals are sampled at $z_n = 0.7\delta$ since the shock is well-defined there. A peak of the correlation is observed at $\tau = -3.3\delta/U_\infty$ (i.e. events are separated by about 3δ) with

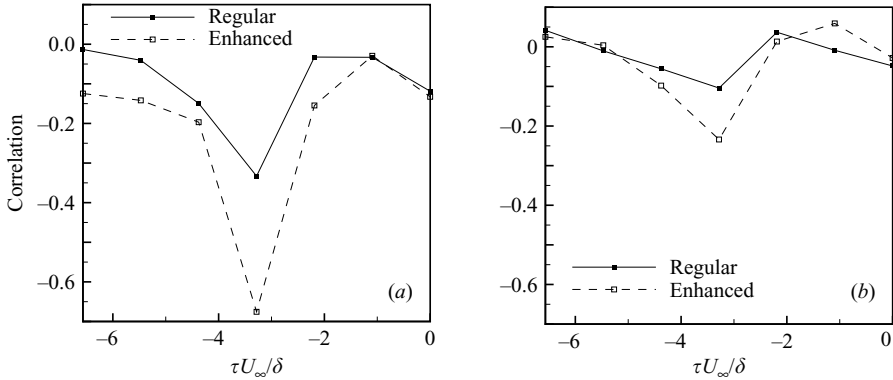


FIGURE 6. Spanwise-averaged correlation with time lag between (a) mass flux at $(x = -5\delta, y, z_n = 0.7\delta)$ and pressure at $(SK_{sm}, y, z_n = 0.7\delta)$, and (b) mass flux at $(x = -5\delta, y, z_n = 0.7\delta)$ and pressure at $(SK_m, y, z_n = 0.7\delta)$.

a magnitude of about 0.35. The ‘enhanced’ correlation is also plotted in figure 6(a), where the contribution to the correlation is only computed if the difference between the instantaneous shock location and SK_{sm} is greater than 0.15δ (or 1.5 standard deviations of the spanwise wrinkling shock motion). In other words, only strong events are accounted for. The enhanced correlation has a similar shape to the regular correlation. It peaks at the same location with a greater magnitude, indicating that the correlation is mainly influenced by strong events. Thus, the spanwise wrinkling is related to low-momentum fluid.

Figure 6(b) plots the correlation between pressure at the absolute mean shock location, SK_m , and the mass flux in the undisturbed incoming boundary layer. For the regular correlation, a peak is observed at the same location as in figure 6(a), but with a much smaller magnitude. The enhanced correlation is also computed, using data only if the instantaneous shock location deviates from SK_m by more than 0.3δ (or 1.5 standard deviations of the streamwise shock motion). Again, the enhanced correlation peaks at the same location; however, the magnitude observed is still much smaller than those in figure 6(a). Measuring the mass flux of the incoming boundary layer in the logarithmic region, where the superstructures are best identified, gives equally low correlation values. Thus, the streamwise shock motion is not significantly affected by low-momentum structures in the incoming boundary layer. Computing the correlations in figure 6 without spanwise averaging gives the same result except that the correlation curve is not as smooth due to the smaller number of samples.

Conditional statistics on the incoming boundary layer have been calculated, conditionally based on the shock being upstream or downstream of the absolute mean location. No significant difference is found in these properties. The conditionally averaged mean profiles and boundary layer parameters (table 1) are nearly identical, with very small difference (consistently less than 3%). This is in agreement with the experiments of Beresh *et al.* (2002) for a 28° compression ramp with $M = 5$, where the difference in the conditionally averaged mean velocity was roughly 2%.

3. Unsteadiness of the separation bubble

The separation and reattachment points (denoted by S and R , respectively) are defined using a $C_f = 0$ criterion. Figure 7(a) plots the time evolution of the

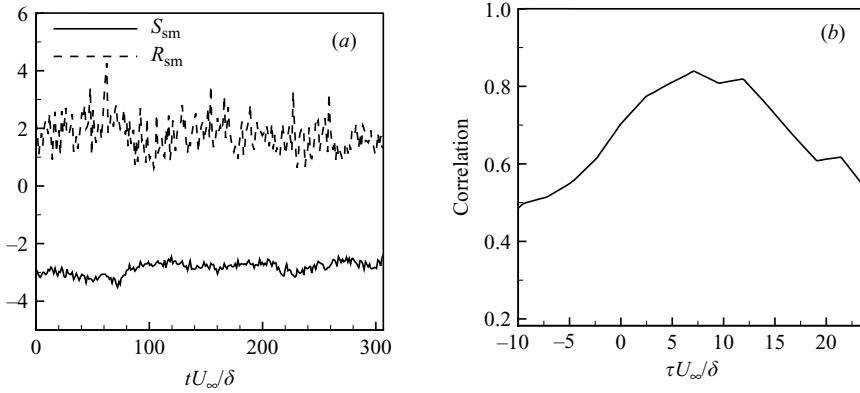


FIGURE 7. (a) Time evolution of the spanwise-mean separation and reattachment points and (b) correlation between the spanwise-mean separation point S_{sm} and shock location SK_{sm} at $z_n = 2\delta$.

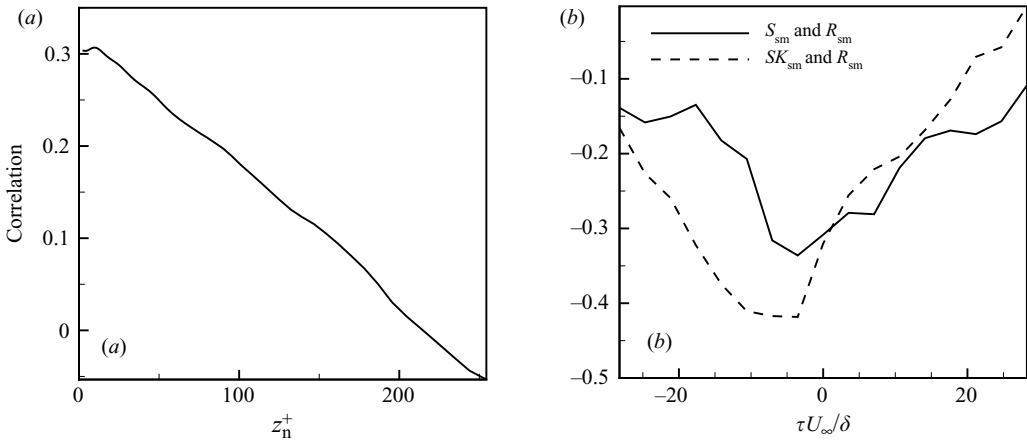


FIGURE 8. (a) Correlation profile between the instantaneous separation point and streamwise-averaged values of ρu and (b) correlation between the separation and reattachment point and the shock location at $z_n = 2\delta$ and the reattachment point.

spanwise-mean separation point S_{sm} and the reattachment point R_{sm} . The spectra for these signals also exhibit a low-frequency component of about $0.01U_\infty/\delta$. The shock foot is related to the separation point because the flow turns first near the separation bubble. Thus, we expect a strong correlation between S_{sm} and SK_{sm} . Figure 7(b) plots the correlation for the spanwise-mean separation point S_{sm} and SK_{sm} at $z_n = 2\delta$. The correlation peak is about 0.85 with a time lag of about $7\delta/U_\infty$. The time interval between each data point in figure 7(b) is about $3\delta/U_\infty$, therefore the peak location has $\pm 3\delta/U_\infty$ uncertainty. This uncertainty also applies for all of the following correlations with time lag. Ganapathisubramani, Clemens & Dolling (2007b) correlated the instantaneous separation point S (defined using a velocity threshold criterion) and streamwise-averaged values of streamwise velocity in the incoming boundary layer at $z_n = 0.2\delta$. The same analysis performed here yields a correlation of about 0.5, which is similar to the value 0.4 found by Ganapathisubramani *et al.* (2007b). Figure 8(a) plots the profile for the correlation between the instantaneous

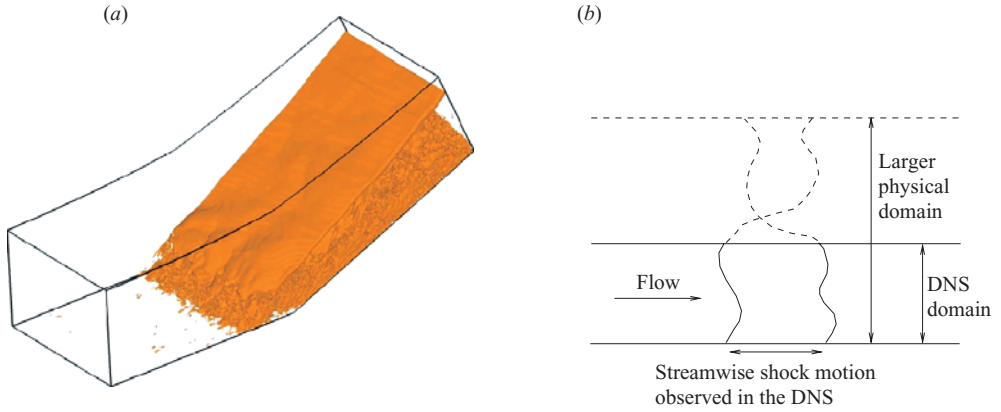


FIGURE 9. (a) $|\nabla p| = 0.5p_\infty/\delta$ showing the structure of the shock in the 4δ spanwise domain DNS case and (b) sketch of possible shock motion pattern in a domain with a larger spanwise extent.

separation point using the $C_f = 0$ definition and streamwise-averaged values of ρu , where the streamwise averaging is performed from the separation point to the inlet. Using the $C_f = 0$ criterion, the correlation factor at $z_n = 0.2$ is 0.23. Thus, the use of the actual definition of the separation point decreases the correlation between the separation point and the streamwise-averaged u significantly.

Figure 8(b) plots two correlations: between S_{sm} and R_{sm} and between the shock location SK_{sm} and R_{sm} . A negative correlation between S_{sm} and R_{sm} is observed, indicating that the separation bubble undergoes a contraction/expansion motion. Moreover, the peaks for both correlations are located at negative time lags, indicating that the motion of the separation point (and the shock) lags that of the reattachment point. This implies that the shock unsteadiness may be caused by the flow inside the separation region, downstream of the shock.

4. Discussion

The DNS data show that the low-frequency shock motion is a streamwise displacement of the shock that is nearly uniform in the spanwise direction. To investigate the effect of domain size, a DNS with a 4δ spanwise domain has been performed. Figure 9(a) shows that the instantaneous shock structure is similar to that of the case with a 2δ spanwise domain. This result does not exclude the possibility of large-wavelength low-frequency spanwise shock wrinkles, as sketched in figure 9(b). If that were the case, from the DNS results one could infer that these events must have a spanwise extent larger than 4δ . Figure 10 shows sequential planform images from filtered Rayleigh scattering of Mach 2.5 flow over a 24° wedge at $Re_\theta = 14000$ from the experiments of Wu (2000) and Wu & Miles (2001). The images are taken at $z_n = 0.9\delta$. The frame size corresponds to $4\delta \times 4\delta$, and the frame rate is 500 kHz, corresponding to about $5U_\infty/\delta$. In this time scale a structure upstream (enclosed by the circle in the first frame) flows through the shock wave. The resulting low-amplitude spanwise wrinkling of the shock by the passing of the eddy is apparent. In addition, a large-amplitude large-wavelength spanwise wrinkling can be observed in all frames, with characteristic wavelength greater than 4δ . These experimental visualizations are in agreement with the DNS data analyses.

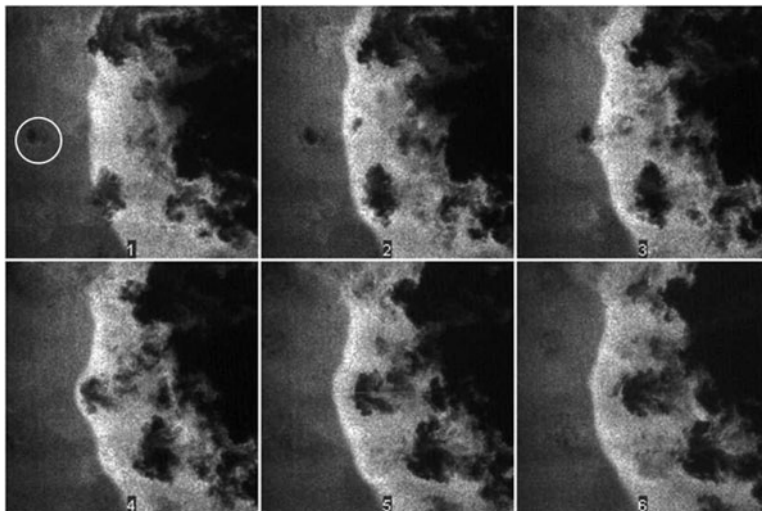


FIGURE 10. Sequential planform images at $z_n = 0.9\delta$ from filtered Rayleigh scattering of Mach 2.5 flow over 24° wedge at $Re_\theta = 14,000$ from the experiments of Wu (2000) and Wu & Miles (2001). Printed with permission.

Regarding the causes of the shock unsteadiness, the local spanwise wrinkling shock motion is shown to correlate with low-momentum fluid in the incoming boundary layer, which is consistent with what Wu & Miles (2001) found in a compression ramp interaction using high-speed visualization techniques. However, the spanwise wrinkling is a smaller-scale local unsteadiness compared with the streamwise shock motion. The small correlation between the low-momentum fluid in the incoming boundary layer and the separation point found in the DNS implies that these low-momentum structures make a relatively minor contribution to the shock unsteadiness. The negative time lag in the correlation between the shock location and reattachment point suggests that the separation region may play an important role in driving the low-frequency shock unsteadiness, as seen experimentally by Thomas *et al.* (1994). The fact that the Strouhal number of the low-frequency shock motion defined using the mean separation bubble length lies in the experimental range (Dussauge *et al.* 2006) also supports this argument. Pirozzoli & Grasso (2006) performed a DNS of a reflected shock interaction and proposed that the shock unsteadiness was sustained by an acoustic resonance mechanism that is responsible for generating tones in cavity flows. However, the low-frequency shock motion may not be captured in their DNS because the lowest Strouhal number reported is between 0.09 and 0.24, which is above the range 0.02–0.05 found in experiments. According to Dussauge *et al.* (2006), the Strouhal number of the low-frequency motion does not seem to have a significant dependence on Mach number, suggesting that acoustic resonance may not cause the low-frequency shock motion. It is interesting to point out that in cavity flows, two modes are observed (Gharib & Roshko 1987; Rowley, Colonius & Basu 2002): the shear-layer mode and the wake mode. In this case, acoustic resonance is responsible for the generation of the shear-layer mode, while the wake mode is purely hydrodynamic. Moreover, the wake mode corresponds to larger-scale and lower-frequency motions than the shear-layer mode. Providing that there are some similarities between compression ramp interactions and cavity flows, in that they all have a shear layer formed above a separated region, we suggest that the mechanism

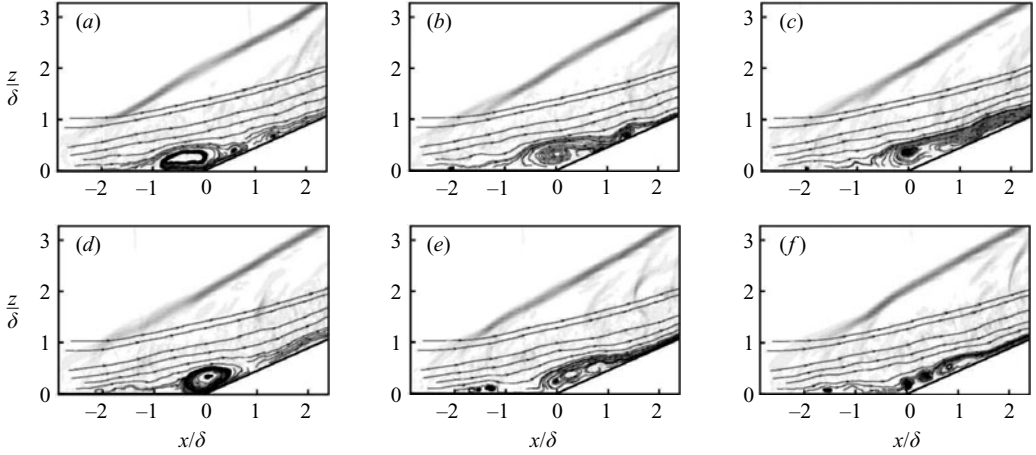


FIGURE 11. Streamlines in (x, z) -planes showing breakdown of the separation bubble. Pressure gradient contours showing the shock location. Time intervals are about $1\delta/U_\infty$.

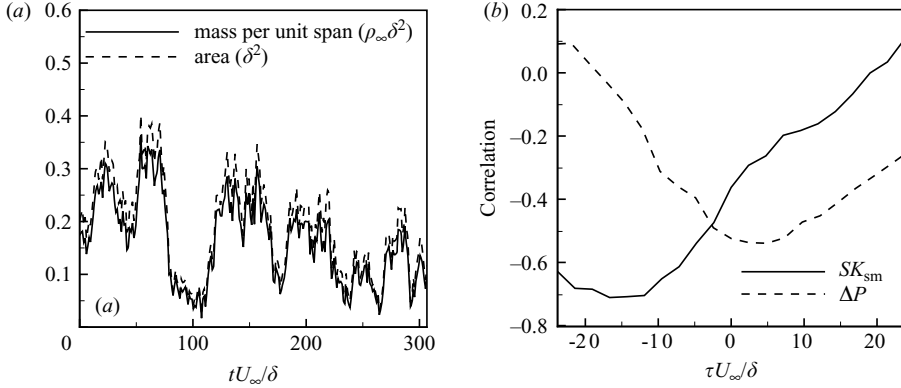


FIGURE 12. (a) Mass and volume of the reverse flow region versus time. (b) Correlation between the mass inside the reverse flow region with the spanwise mean shock location SK_{sm} at $z = 2\delta$ and with the wall pressure difference $\Delta P = P_w(x = 1\delta) - P_w(x = -2\delta)$.

of the low-frequency shock unsteadiness may resemble that of the generation of the wake mode in cavity flows. In other separated flows, for example flow passing a backward-facing step, low-frequency fluctuations have also been indicated (e.g Simpson 1989), while the driving mechanisms are still not fully understood.

DNS data animations show that the size (including the length and height) of the separation bubble changes significant with a low frequency that is comparable to that of the low-frequency shock motion. Figure 11 plots six consecutive times in the DNS with time intervals of about δ/U_∞ , showing the breakdown of the separation bubble indicated by streamlines. Flow quantities are averaged in the spanwise direction to give a clear picture. Contours of pressure gradient are also plotted to show the shock location. From frames (c) to (f), fluid bursts outside the separation bubble, causing the bubble to shrink. The shock then moves downstream at a later time (not seen in the figure). To show how the separation bubble changes with time, the mass and the area of the reverse flow region inside the separation bubble are plotted in figure 12(a). The reverse flow region is defined as a region in which u is negative,

where u is spanwise averaged. It is observed that the mass inside the reverse flow region has an intermittent character, like the momentum signal inside the shock motion region shown in figure 4. Figure 12(b) plots the correlation of the mass signal with the spanwise-averaged shock location at $z = 2\delta$. A high peak of 0.7 is observed at about $\tau = -13\delta/U_\infty$, showing that the shock motion is closely related to that of the separation bubble. In addition, the shock motion lags that of the separation bubble, indicating that the separation bubble drives the shock motion. Also, figure 12(b) plots the correlation of the mass signal with the pressure difference between $x = 1\delta$ and $x = -2\delta$, which are close to the reattachment and separation points, respectively. The pressure gradient decreases with increasing mass of reverse flow, which is due to the enlargement of the separation bubble in the streamwise direction and decreasing of streamline curvature.

Based on the above observations, it is hypothesized that one of the mechanisms driving the low-frequency shock motion can be described as a feedback loop between the separation bubble, the separated shear layer and the shock system, which has some similarities with the cause of the low-frequency ‘flapping motion’ in backward-facing step flows described by Eaton & Johnston (1981). That is, the balance between shear layer entrainment from the separation bubble and injection near the reattachment point is perturbed. If the injection is greater, the separation bubble grows in size and causes the reattachment point to move downstream and the separation point to move upstream. The motion of the separation point causes the shock to move with it. As the shock moves upstream, the pressure gradient in the separation region decreases due to the enlargement of the separation region and decreasing of streamline curvature. The decreasing pressure gradient reduces the entrainment of fluid into the separation bubble. In turn, the separation bubble becomes unstable and breaks down. When this happens, fluid bursts outside the bubble and the separation region shrinks fairly rapidly, causing the shock to move downstream at a later time. Similarly, when the shock moves to a downstream location, the overall pressure gradient in the separation region increases, which enhances entrainment of fluid into the separation bubble, causing the bubble to grow. Thus, the low-frequency shock motion is closely related to the time scale associated with the growth and burst of the separation bubble. Assuming that this time scale is determined by the length of the separation bubble L and the characteristic speed of the reverse flow U_R , the dimensionless shock frequency $St_R = fL/U_R$ can be computed. Using the maximum of the time-averaged reverse flow speed in the separation bubble, $0.055U_\infty$, to represent U_R , the dimensionless frequency St_R in the DNS is around unity (about 0.8).

5. Conclusion

Wall-pressure and separation-point signals indicate low-frequency motions in DNS data of a 24° compression ramp. Analyses show that the shock motion is characterized by a low-frequency large-amplitude streamwise motion with characteristic frequency of about $0.013U_\infty/\delta$, and a relatively small-amplitude high-frequency $O(U_\infty/\delta)$ spanwise wrinkling. The mass flux in the incoming boundary layer is correlated with the high-frequency spanwise wrinkling motion. Conditional statistics indicate no significant difference in the mean properties of the incoming boundary layer when the shock is upstream/downstream.

The location of the separation point is highly correlated with the shock location at $z_n = 2\delta$ with a time lag of about $7\delta/U_\infty$. A small correlation is found between the low-momentum structures in the incoming boundary layer and the separation

point, indicating that the influence of the superstructures on the shock motion may be minor. However, it is found that both the shock motion and the separation-point motion are correlated with and lag the motion of the reattachment point, suggesting that the downstream flow plays an important role in driving the low-frequency shock motion. These findings are different to those noted in the experimental investigations by Ganapathisubramani *et al.* (2007a). A model that is described as a feedback loop between the separation bubble, the separated shear layer, and the shock system is proposed to explain the low-frequency shock motion. Using the length of the mean separation bubble and the characteristic reverse flow speed (e.g. the maximum of the mean reverse flow speed), the Strouhal number of the low-frequency shock motion is around unity.

We acknowledge insightful discussions with A. J. Smits and the support from the Air Force Office of Scientific Research under grant no. AF/9550-06-1-0323.

REFERENCES

- ANDREOPOULOS, J. & MUCK, K. C. 1987 Some new aspects of the shock-wave/boundary-layer interaction in compression-ramp flows. *J. Fluid Mech.* **180**, 405–428.
- BERESH, S. J., CLEMENS, N. T. & DOLLING, D. S. 2002 Relationship between upstream turbulent boundary-layer velocity fluctuations and separation shock unsteadiness. *AIAA J.* **40**, 2412–2423.
- BOOKEY, P. B., WYCKHAM, C., SMITS, A. J. & MARTIN, M. P. 2005 New experimental data of STBLI at DNS/LES accessible Reynolds numbers. *AIAA Paper* 2005-309.
- DOLLING, D. S. & OR, C. T. 1985 Unsteadiness of the shock wave structure in attached and separated compression ramp flows. *Exp. Fluids* **3**, 24–32.
- DUPONT, P., HADDAD, C. & DEBIÈVE, J. F. 2006 Space and time organization in a shock-induced separated boundary layer. *J. Fluid Mech.* **559**, 255–277.
- DUSSAUGE, J. P., DUPONT, P. & DEBIÈVE, J. F. 2006 Unsteadiness in shock wave boundary layer interactions with separation. *Aerospace Sci. Tech.* **10** (2).
- EATON, J. K. & JOHNSTON, J. P. 1981 Low-frequency unsteadiness of a reattaching turbulent shear layer. In *Proc. 3rd Int. Symp. on Turbulent Shear Flow*. Springer.
- ERENGIL, M. E. & DOLLING, D. S. 1991 Correlation of separation shock motion with pressure fluctuations in the incoming boundary layer. *AIAA J.* **29**, 1868–1877.
- GANAPATHISUBRAMANI, B., CLEMENS, N. T. & DOLLING, D. S. 2006 Large-scale motions in a supersonic turbulent boundary layer. *J. Fluid Mech.* **556**, 271–282.
- GANAPATHISUBRAMANI, B., CLEMENS, N. T. & DOLLING, D. S. 2007a Effects of upstream boundary layer on the unsteadiness of shock induced separation. *J. Fluid Mech.* **585**, 369–394 .
- GANAPATHISUBRAMANI, B., CLEMENS, N. T. & DOLLING, D. S. 2007b Effects of upstream coherent structures on low-frequency motion of shock-induced turbulent separation. *AIAA Paper*. 2007-1141.
- GHARIB, M. & ROSHKO, A. 1987 The effect of flow oscillations on cavity drag. *J. Fluid Mech.* **177**, 501–530.
- HUTCHINS, N. & MARUSIC, I. 2007 Evidence of very long meandering features in the logarithmic region of turbulent boundary layers. *J. Fluid Mech.* **579**, 1–28.
- OWEN, F. K. & HORSTMANN, C. C. 1972 On the structure of hypersonic turbulent boundary layers. *J. Fluid Mech.* **53**, 611–636.
- PIROZZOLI, S. & GRASSO, F. 2006 Direct numerical simulation of impinging shock wave/turbulent boundary layer interaction at $M = 2.25$. *Phys. Fluids* **18**.
- PLOTKIN, K. J. 1975 Shock wave oscillation driven by turbulent boundary-layer fluctuations. *AIAA J.* **13**, 1036–1040.
- RINGUETTE, M. J., WU, M. & MARTIN, M. P. 2008 Coherent structures in direct numerical simulation of supersonic turbulent boundary layers at Mach 3. *J. Fluid Mech.* **594**, 59–69.
- ROWLEY, C. W., COLONIUS, T. & BASU, A. J. 2002 On self-sustained oscillation in two-dimensional compressible flow over rectangular cavities. *J. Fluid Mech.* **455**, 315–346.

- SAMIMY, M., ARNETTE, S. A. & ELLIOTT, G. S. 1994 Streamwise structures in a turbulent supersonic boundary layer. *Phys. Fluids* **6**, 1081–1083.
- SELIG, M. S. 1988 Unsteadiness of shock wave/turbulent boundary layer interactions with dynamic control. PhD thesis, Princeton University.
- SIMPSON, R. L. 1989 Turbulent boundary-layer separation. *Ann. Rev. Fluid Mech.* **21**, 205–234.
- THOMAS, F. O., PUTNAM, C. M. & CHU, H. C. 1994 One the mechanism of unsteady shock oscillation in shock wave/turbulent boundary layer interactions. *Exps. Fluids* **18**, 69–81.
- WU, M. & MARTIN, M. P. 2007 Direct numerical simulation of shockwave and turbulent boundary layer interaction induced by a compression Ramp. *AIAA J.* **45**, 879–889.
- WU, P. 2000 MHz-rate pulse-burst laser imaging system: development and application in the high-speed flow diagnostics. PhD thesis, Princeton University.
- WU, P. & MILES, R. B. 2001 Megahertz visualization of compression-corner shock structures. *AIAA J.* **39**, 1542–1546.